Combining UAV and Sentinel-2 satellite multi-spectral images to diagnose crop growth and N status in winter wheat at the county scale

Jie Jiang[a, b, c, d, e], Peter M. Atkinson[f, g, h], Chunsheng Chen[i], Qiang Cao[a, b, c, d, e], Yongchao Tian[a, b, c, d, e], Yan Zhu[a, b, c, d, e], Xiaojun Liu[a, b, c, d, e*], Weixing Cao[a, b, c, d, e*]

[a] National Engineering and Technology Center for Information Agriculture, Nanjing Agricultural University, Nanjing 210095, China

[b] MOE Engineering Research Center of Smart Agricultural, Nanjing Agricultural University, Nanjing 210095, China

[c] MARA Key Laboratory for Crop System Analysis and Decision Making, Nanjing Agricultural University, Nanjing 210095, China

[d] Jiangsu Key laboratory for Information Agriculture, Nanjing Agricultural University, Nanjing 210095, China

[e] Institute of Smart Agriculture, Nanjing Agricultural University, Nanjing 210095, China

[f] Faculty of Science and Technology, Lancaster University, Lancaster LA1 4YR, UK

[g] Geography and Environmental Science, University of Southampton, Highfield, Southampton SO17 1BJ, UK

[h] Institute of Geographic Sciences and Natural Resources Research, Chinese Academy of Sciences, 11A Datun Road, Beijing 100101, China

[i] Xinghua Extension Centre for Agricultural Technology, Taizhou 225700, China

*Correspondence: liuxj@njau.edu.cn (X. Liu), caow@njau.edu.cn (W. Cao); Tel.: +86-25-8439-6804; Fax: +86-25-8439-6672

Abstract:

Real-time and non-destructive nitrogen (N) status diagnosis is needed to support in-season N management decision-making for modern wheat production. For this purpose, satellite sensor imaging can act as an effective tool for collecting crop growth information across large areas, but they can be challenging to calibrate with ground reference data. This research aimed to calibrate satellite remote sensing-derived models for crop growth estimation and N status diagnosis based on fine-resolution unmanned aerial vehicle (UAV) images, thus, map wheat growth and N status at the county scale. Seven wheat field experiments involving multi cultivars and different N applications were conducted at four farms of Xinghua county from 2017 to 2021. A fixed-wing UAV sensing system and the Sentinel 2 (S2) satellite were used to collect wheat canopy multispectral images; three growth variables (plant dry matter (PDM), plant N accumulation (PNA) and N nutrition index (NNI)) and weather data, synchronized with spectral imagery, were obtained at the jointing and booting stages. The farm- scale PDM (UAV-PDM) and PNA (UAV-PNA) maps can be derived from the UAV images at the four farms, which were further upscaled to grids to match the S2 image resolution using pixel aggregation method. Then, satellite- based prediction models were constructed by fitting four machine learning algorithms to the relationships be-tween satellite spectral indices, upscaled PDM (PNA) and weather data. Amongst the four methods tested, the random forest (RF) achieved the greatest prediction accuracy for PDM (R^2 = 0.69–0.93) and PNA (R^2 = 0.60–0.77). Meanwhile, an indirect diagnosis method was used to calculate the NNI. The results indicated that the model derived from the S2 imagery performed well for predicting NNI (R^2 = 0.46–0.54) at the jointing and booting stages. Thereby, the NNI was used to map winter wheat N nutrition status at the county scale. In summary, this research demonstrated and evaluated an approach to combine UAV and satellite sensor images to diagnose wheat growth and N status across large areas.

Key words: N diagnosis, pixel aggregation, vegetation index, random forest, large areas

1. Introduction

Wheat is one of the important crops that widely cultivated in the world, which plays a vital role in ensuring the world food security. The area covered by wheat in China is the fourth with 11% proportion of the global plantation area, while the wheat yield accounts for appropriate 18% of the total yield in the world (Li et al., 2016; Wu et al., 2022). Nitrogen (N) has a significant effect in enhancing crop growth and improving grain yield formation (Miao et al., 2011). A precision N management strategy (PNMS) can be used to optimize N fertilizer inputs and maximize the economic benefits for producers. Such a PNMS re-quires non-destructive and effective tools for crop growth prediction and N status diagnosis (Diacono et al., 2013).

Traditional N diagnosis methods such as leaf color-based judgement and chemical analysis based for measured plant sample were relatively empirical or time-consuming for evaluating the plant N nutrition status, which may not be sufficient to support making in-season real-time N management decisions in modern crop production (Padilla et al., 2018). At the same time, remote sensing technologies provide a non-destructive approach for real-time diagnosis of crop growth and N status (Moya, 2005;

Dong et al., 2019). Ground sensing based on proximal sensors has been used to predict plant biomass and N accumulation for various crops, including rice, wheat and maize (Xia et al., 2016; Jiang et al., 2020; Zhang et al., 2020). However, the small sampling area of ground sensors makes this approach laborious for crop growth estimation and N diagnosis at regional scales. Satellite remote sensing can perform spectral sampling for crop N status estimation over large areas, and is likely to be more suitable for guiding regional crop N management (Magney et al., 2017). Common satellite missions were classified according to the spatial resolution: coarse spatial resolution satellite sensors such as MODIS (spatial resolution ≥ 250 m) have been used for monitoring vegetation productivity and mapping foliar N in forests at broad scales (Guay et al., 2014; Lepine et al., 2016). However, images with coarse resolution are insufficient to detect field heterogeneity due to the lack of pure pixels during the crop growth period (Lepine et al., 2016). Rapideye and IKONOS satellite sensors can produce images with a fine spatial resolution of 1 m, which have been used for academic research and agricultural production when combined with easy access to compute resource (Rinaldi et al., 2010; Magney et al., 2017). Wang et al. (2019) indicated that vegetation indices such as normalised difference vegetation index (NDVI) and normalised difference red edge (NDRE) derived from RapidEye images achieved good precision (R^2 >0.6) for predicting wheat grain N uptake during the grain filling stage. However, the cost of fine-resolution images has limited their practical application in modern crop production. Freely available medium-to-fine resolution satellite sensor images from Sentinel-2 (S2) have been more popular with researchers conducting regional studies for crop N management. Meanwhile, the revisit period of 5 days of S2 makes it suitable for real-time estimation and diagnosis of crop growth and N status. There-fore, the advantages of free-access and high revisit rate from the S2 satellite sensor imagery were more beneficial for facilitating the practical agricultural production. Sharifi (2020) indicated that the simple ratio red-edge (SRRE) index derived from the S2 satellite sensor image has a good performance for estimating maize N uptake with R^2 of 0.91 and RMSE of 11.34 kg ha^{-1} at the peak greenness date. Additionally, the normalized difference red edge index (NDRE) and transformed chlorophyll absorption ratio index (TCARI) from the S2 images were demonstrated a good linear estimates for maize NNI (R^2 = 0.79) and durum wheat NNI (R^2 = 0.61), respectively (Crema et al., 2020). Therefore, it is necessary to further evaluate the utility of spectral information derived from the S2 satellite sensor images with medium-to-fine resolution for wheat growth estimation and N status diagnosis.

Previous studies calibrated satellite-based models for crop growth estimation mainly through single or multiple field measurements, which are laborious and difficult to upscale to the same spatial resolution as the satellite sensor images (Huang et al., 2017). UAV-based remote sensing systems can be operated with ease and have been demonstrated to be excellent tools for diagnosing crop N status (Zhao et al., 2019). Furthermore, the fine-resolution images from UAVs can detect field heterogeneity and can be aggregated to grids with any desired resolution. Thus, UAVs offer an opportunity to close the gap between field measurements and satellite sensor data. Revill et al. (2020) coupled S2 and UAV observations to bridge the scaling gap between field data and satellite sensor images, and the results indicated this method achieved an accurate retrieval for wheat leaf area index across a large farm. Similarly, the fractional cover (FCover) of tundra vegetation derived from a fine-resolution UAV RGB image was aggregated to corresponding grids with same spatial resolution as Planet (3 m), S2 (10 m, 20 m) and Landsat 8 (30 m) images. Therefore, the FCover prediction model based on satellite imagery can be constructed using the relationship between UAV-FCover and satellite vegetation indices (Deviance explained =89% at best) over larger extents (Riihima¨ki et al., 2019). To date, little research has been performed on the integration of fixed-wing UAVs and satellite sensor images to diagnose the growth and N status of winter wheat at the county scale. Therefore, the objectives of this study were: (1) to bridge the scale gap between field observed wheat growth parameters and satellite sensor data based on fine-resolution UAV images; (2) to construct wheat growth estimation and N diagnosis models using S2 satellite sensor images and (3) to map wheat growth and N status temporally and spatially at the county scale.

2. Materials and methods

2.1. Experimental design

This study was conducted at the Xinghua experimental station in Jiangsu Province of East China (Fig. 1). Experiment 1–3 were conducted using ‘Yangmai 23′ and ‘Yangmai 25′ cultivar at the Diaoyu farm from 2017 to 2020. Experiment 4 was conducted using ‘Nongmai 88′ cultivar at the Daiyao farm in 2019–2020. Experiment 5 and 6 were conducted using ‘Yangmai 25′ at the Daduo and Zhouzhuang farm, respectively, in 2019–2020. Experiment 7 was conducted based on the local cultivar such as ‘Yangmai 23′, ‘Yangmai 25′ and ‘Nongmai 88′ across the Xinghua county in 2020–2021. The fertilizer treatments of experiment 1–7 fol-lowed the local farmer’ conventional approach, which were showed in Table S1 of the Supplymentary file. Wheat plants in experiments 1–7 were grown at a local standard density of 2.25 million seedlings per hectare. Irrigation application was applied one time to ensure the seeds germinated securely at the sowing stage if there was no natural rainfall. The weather data was collected from the local weather station, the Fig. 2 showed the accumulated precipitation, daily average temperature and accumulated radiation with days after sowing during the whole wheat growing season from 2017 to 2021. No significant insects, weeds and water stress were observed through the whole growing season. Details of the seven wheat experiments were shown in Table 1.

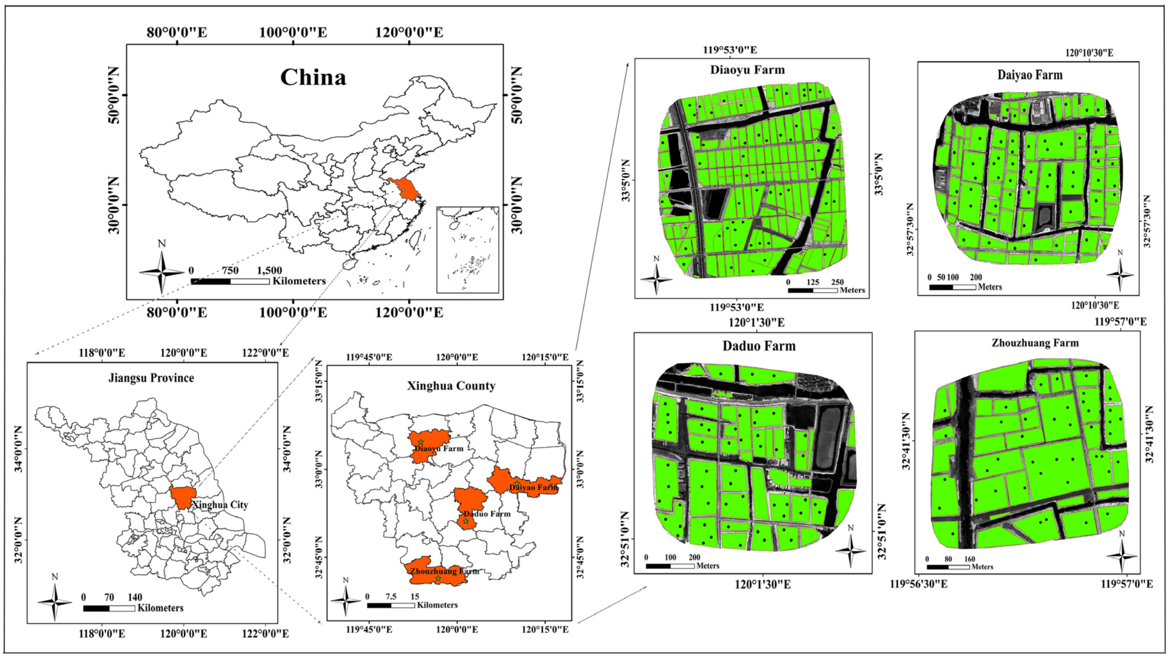

Fig. 1. The four study sites. The green areas and black points indicate the wheat growing area and sampling points, respectively, in each farm.

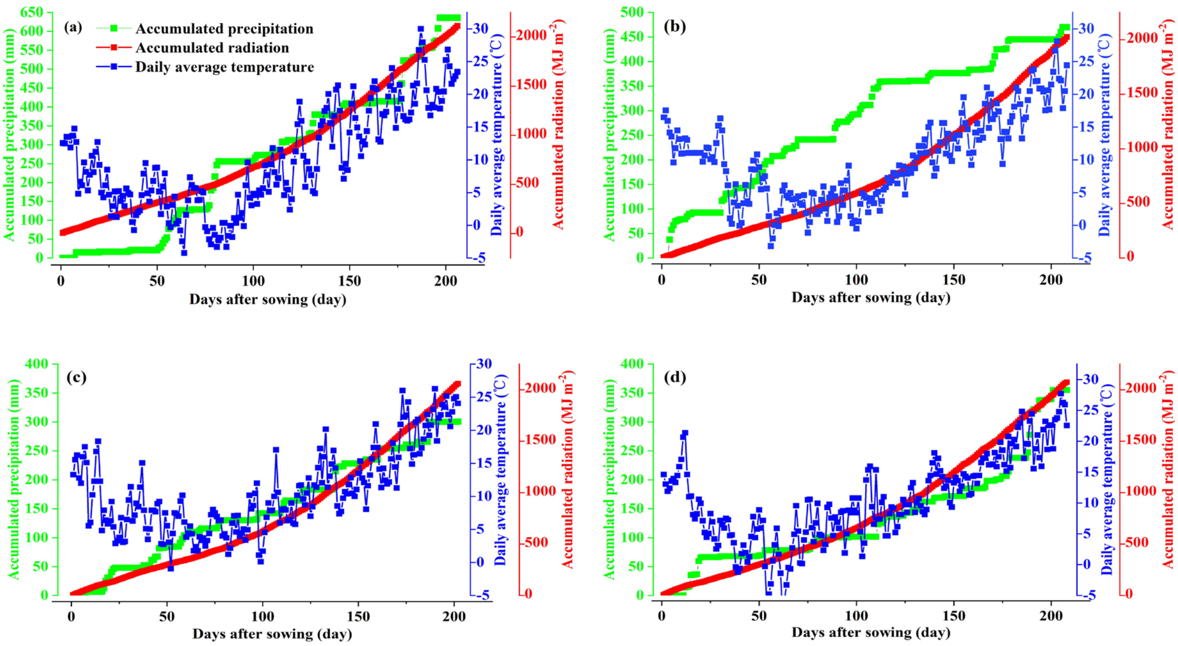

Fig. 2. Accumulated precipitation, daily average temperature and accumulated radiation with days after sowing during the whole wheat growing season of (a) 2017–2018, (b) 2018–2019, (c) 2019–2020, (d) 2020–2021 in Xinghua experimental station.

Table 1 Basic information describing the seven field experiments conducted in this study.

Experiment No. Year	Location	Cultivar	UAV image acquisition time	S2 image acquisition time	Plant sampling date	Sowing date	Harvest date
Experiment 1 2017-2018	Diaoyu farm (33.08°N, 119.98°E)	YM 23	22-March (JS) 16-April (BS)	23-March (JS)	None	9 Nov.	3 June
Experiment 2 2018-2019	Diaoyu farm (33.08°N, 119.98°E)	YM 25	6-March (JS) 2-April (BS)	6-March (JS) 30-March (BS)	None	2 Nov.	29 May
Experiment 3 2019-2020	Diaoyu farm (33.08°N, 119.98°E)	YM 25	16-March (JS) 2-April (BS)	17-March (JS) 3-April (BS)	None	9 Nov.	2 June
Experiment 4 2019-2020	Daiyao farm (32.96°N, 120.17°E)	NM 88	19-March (JS) 6-April (BS)	24-March (JS) 8-April (BS)	None	5 Nov.	1 June
Experiment 5 2019-2020	Daduo farm (32.85°N, 120.02°E)	YM 25	20-March (JS) 7-April (BS)	24-March (JS) 8-April (BS)	None	4 Nov.	1 June
Experiment 6 2019-2020	Zhouzhuang farm (32.69°N, 119.95°E)	YM 25	20-March (JS) 6-April (BS)	24-March (JS) 8-April (BS)	None	6 Nov.	2 June
Experiment 7 2020-2021	Xinghua county (32.65-33.25°N, 119.60-120.32°E)	YM 23, YM 25, NM 88	None	14-March (JS) 8-April (BS)	12(14)-March (JS) 8-April (BS) 31-May to 2-June (HS)	25 Oct.- 10 Nov.	29 May- 10 June

Note: the YM23, YM25 and NM 88 represent the Yangmai 23, Yangmai 25 and Nongmai 88 cultivars, respectively. JS, BS and HS represent the jointing, booting and harvest stages, respectively. The S2 image was not available at the booting stage in experiment 1.

2.2. Spectral data collection

2.2.1. UAV images collection

The Parrot Sequoia camera (MicaSense, Seattle, WA, USA; Fig. 3) was mounted on the eBee UAV (senseFly, Cheseaux-Lausanne, Switzerland; Fig. 3) to collect four multispectral images, including the green (G, 550 ± 40 nm), red (R, 660 ± 40 nm), red edge (RE, 735 ± 10 nm) and near infrared (NIR, 790 ± 40 nm) bands. The parameter setting of the UAV flights and pre-processing method of the multispectral images followed Jiang et al. (2022). UAV flight was conducted at a speed of 8 m s^{-1} under stable low wind, cloudless and sunny-sky conditions from 10:00 to 14:00. The overlap in the flight direction and sidelap were set as 75% for each image. The spatial resolution of spectral image was 10 cm when the flight height was 100 meters above the wheat canopy. The radiation calibration and mosaicking of the acquired images were performed in the Pix4Dmapper Ag software (Pix4D SA, Prilly, Switzerland). Several ground control points (GCPs) were located using a Trimble GeoXH6000, which were then used to geo-rectify the UAV orthographic image for each farm. Details of UAV image acquisition times were shown in Table 1.

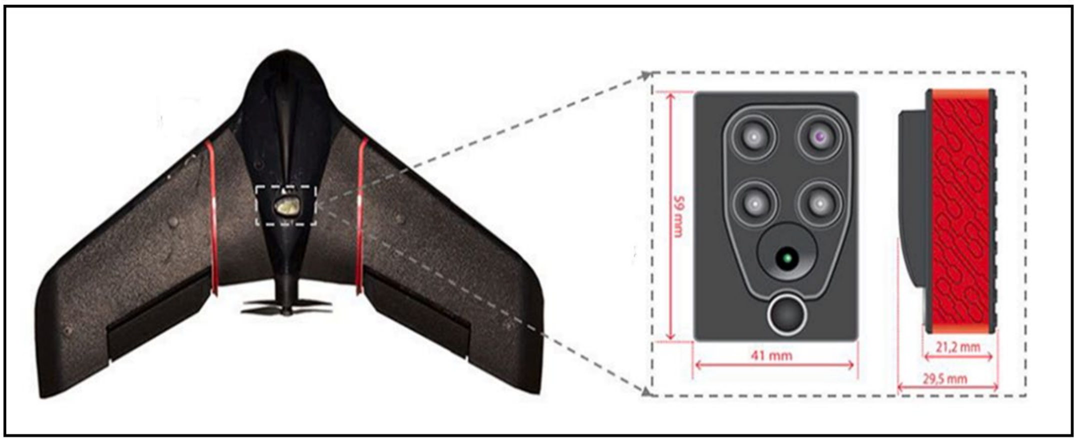

Fig. 3. The eBee fixed-wing UAV used in this study.

2.2.2. Sentinel 2 images acquisition

The satellite sensor imagery was acquired as close as possible to the UAV flights, with a screening criteria of five days adjacent to the UAV campaign. Sentinel 2 images can be downloaded from the official website (https://scihub.copernicus.eu/) as Level-1C geometrically corrected, top-of-atmosphere reflectance products. The atmospheric correction was carried out using the Sen2Cor version 02.08.00 to produce the Level-2A product. The plug-in of 'SuperResolution' in Sentinel Application Platform (SNAP) version 4.0.2 was used to downscale the Level-2A image bands with 20 m spatial resolution to 10 m resolution. Each S2 image include 13 bands (Table 2) with 290 km orbital swath width: three bands were designed for monitoring atmospheric conditions with 60 m spatial resolution (B1, B10, B11), which were not considered in this research. Meanwhile, the red edge (RE) band b5 was selected among the three RE bands, the Narrow NIR band b9 was selected between the two NIR bands and the SWIR band b12 was selected between the two SWIR bands. The six selected bands were used to calculate the spectral indices in Table 3.

Table 2 The 13 spectral bands from the S2 satellite sensor image.

Bands		Central wavelength	Bandwidth	Spatial resolution
Band 1	Coastal aerosol	443	20	60
Band 2	**Blue**	**490**	**65**	**10**
Band 3	**Green**	**560**	**35**	**10**
Band 4	**Red**	**665**	**30**	**10**
Band 5	**Red edge**	**705**	**15**	**20**
Band 6	Red edge	740	15	20
Band 7	Red edge	783	20	20
Band 8	NIR	842	115	10
Band 9	**Narrow NIR**	**865**	**20**	**20**
Band 10	Water vapor	945	20	60
Band 11	SWIR-Cirrus	1380	30	60
Band 12	**SWIR**	**1610**	**90**	**20**
Band 13	SWIR	2190	180	20

Table 3 The vegetation indices used in this research.

Index name	Formula	S2	UAV	Reference
Normalised difference red edge (NDRE)	(NIR - RE)/(NIR + RE)	√	√	(Barnes et al., 2000)
Red edge soil-adjusted vegetation index (RESAVI)	1.5*(NIR - RE)/(NIR + RE + 0.5)	√	√	(Sripada et al., 2005)
Red edge chlorophyll index (CIRE)	(NIR / RE) - 1	√	√	(Sripada et al., 2005)
DATT	(NIR - RE) / (NIR - Red)	√	√	(Datt and B., 2010)
Modified chlorophyll absorption in reflectance index (MCARI1)	[(NIR - RE) − 0.2(NIR - G)] *(NIR / RE)	√	√	(Gitelson et al., 2005)
Ratio water index (RWI)	NIR / SWIR	√		(Fernandes et al., 2003)
Normalized difference water index (NDWI)	(NIR - SWIR) / (NIR + SWIR)	√		(Gao, 1995)
Ratio blue index (RBI)	NIR / B	√		(This study, modified from Pearson and Miller, 1972)
Normalised difference blue index (NDBI)	(NIR - B) / (NIR + B)	√		(This study, modified from Tucker, 1979)
Green soil adjusted vegetation index (GSAVI)	1.5*(NIR - G)/(NIR + G + 0.5)	√	√	(Sripada et al., 2005)
Soil adjusted vegetation index (SAVI)	1.5*(NIR - Red)/(NIR + Red + 0.5)	√		(Huete, 1988)
Normalised difference vegetation index (NDVI)	(NIR - Red)/(NIR + Red)	√	√	(Tucker, 1979)
Ratio vegetation index (RVI)	NIR / Red	√		(Pearson and Miller, 1972)

Note: √ represents the vegetation indices calculated based on the satellite and UAV images.

2.3. Agronomic and weather data collection

The GPS coordinates of each sampling point was determined by a Trimble GeoXH6000 (Trimble, CA, USA). Then, 20 plants were selected randomly and sampled within a range of 10*10 m centered around the sampling point. The plants were separated into the stem and leaf, which were oven dried at 105° for 30 minutes and then dried at 70° to a constant weight to measure the stem dry matter (SDM) and leaf dry matter (LDM). The plant dry matter (PDM) was calculated by equation 1.

$$\mathrm{PDM}\ (\mathrm{kg} \cdot \mathrm{ha}^{-1}) = \mathrm{SDM}\ (\mathrm{kg} \cdot \mathrm{ha}^{-1}) + \mathrm{LDM}\ (\mathrm{kg} \cdot \mathrm{ha}^{-1}) \quad (1)$$

The sub-samples of stem and leaf were later ground into a fine powder to determine the stem (SNC) and leaf (LNC) N concentration using the Kjeldahl digestion method (Bremner and Mulvaney, 1982). The PNA was then calculated by equation 2. The plant N concentration (N_a) can be calculated as the ratio of PNA and PDM.

$$\mathrm{PNA}(\mathrm{kg} \cdot \mathrm{ha}^{-1}) = \mathrm{SDM}(\mathrm{kg} \cdot \mathrm{ha}^{-1}) \times \mathrm{SNC}(\%) + \mathrm{LDM}(\mathrm{kg} \cdot \mathrm{ha}^{-1}) \times \mathrm{LNC}(\%) \quad (2)$$

The NNI (equation 3) can be calculated using actual plant N concentration (N_a) divided by critical value, while the critical N concentration (N_c) can be calculated using the critical N dilution curve (CNDC; equation 4) developed by Jiang et al. (2020).

$$\mathrm{NNI} = \mathrm{N}_a/\mathrm{N}_c \quad (3)$$

$$\mathrm{N}_c = 4.17 * \mathrm{W}^{-0.39} \quad (4)$$

where W is the plant biomass.

The grain yield was collected by manually measuring 1 m^2 three times at each sampling points in the harvest stage, and the observed value was standardized to 14% grain moisture content.

Previous studies indicated that weather status would influence crop growth and the physiological process, and so should be included to increase prediction accuracy during model construction (Wang et al., 2020; Nonhebel, 1994; Verma et al., 2003). In this study, average daily temperature (T_{ave}), average daily minimum temperature (T_{min}), average daily maximum temperature (T_{max}), accumulated daily average temperature (T_{sum}), accumulated precipitation ($Prep_{sum}$), accumulated radiation (Rad_{sum}) of 30 days before measurement date, and accumulated growing degree day (AGDD) from sowing to measurement date were used as model inputs to calibrate the growth and N status diagnosis model.

2.4. Data analysis

The workflow for estimation model construction and evaluation was shown in figure 4: when the UAV orthographic images were collected (Fig. 4a), the PDM and PNA estimation models based on the UAV data from Jiang et al. (2022) were used to derive the wheat PDM (UAV-PDM) and PNA (UAV-PNA) maps at each farm for experiments 1-6 (Fig. 4b). Following the method from Riihimäkia et al. (2019), the UAV-PDM and UAV-PNA maps were upscaled to the same spatial resolution as the S2 images (10 m) using the pixel aggregation function of ArcGIS 10.2 software (Fig. 4c). In order to avoid the influence of mixing pixels from the water, road and other objects for model construction, the sampling points of 57, 52, 53, and 43 that involving the pure pixel inner the wheat field were determined randomly at the Diaoyu, Daiyao, Daduo, and Zhouzhang farm, respectively, to extract the upscaled PDM and PNA values (Fig. 4c). Meanwhile, the S2 images from each farm of experiment 1-6 were obtained (Fig. 4d), and the vegetation indices at the corresponding sampling points were extracted from the S2 imagery (Fig. 4e). Therefore, the data from experiments 1-6 and 10-fold cross-validation were used to select the optimal machine learning (ML) modeling method to integrate the S2 spectral indices, weather data (Fig. 4f), and upscaled PDM (PNA) to construct the estimation models (Fig. 4g). The methods considered were the Random Forest (RF), Lasso, artificial neural network (ANN) and partial least squares regression (PLSR). The optimal modelling method with the larger R^2 and smaller root mean square error (RMSE; equation 5) and relative error (RE; equation 6) was selected to establish the optimal satellite models for PDM and PNA prediction. Therefore, the satellite prediction models with best modeling method were established based on the data from experiments 1-6 (Fig. 4h). Independent ground sampling data from the experiment 7 was used to further validate the optimum PDM and PNA estimation models.

$$\mathrm{RMSE}=\sqrt{\frac{1}{\mathrm{n}}\times\sum_{\mathrm{i}=1}^{\mathrm{n}}(\mathrm{P_i}\text{-}\mathrm{O_i})^2} \tag{5}$$

$$\mathrm{RE}(\%)=100\times\sqrt{\frac{1}{\mathrm{n}}\times\sum_{\mathrm{i}=1}^{\mathrm{n}}\left(\frac{\mathrm{P_i}\text{-}\mathrm{O_i}}{\mathrm{O_i}}\right)^2} \tag{6}$$

where n represents the number of samples, O_i and P_i represent the observed and predicted values, respectively.

An indirect strategy (Fig. 4i) was used to estimate the NNI in this study: when the PDM and PNA were predicted, the PDM was input to the CNDC to calculate the N_c, then the PNA_c can be calculated as the product of predicted PDM and N_c. Therefore, the NNI was calculated as ratio of predicted PNA and PNA_c (equation 7; Jiang et al., 2022; Zha et al., 2020; Xia et al., 2016). Three N status categories of N deficient, N optimal, and N excessive can be divided using the predicted NNI according to the optimal NNI diagnosis interval: 0.92-1.04 and 0.97-1.15 at the jointing and booting stage (Jiang et al., 2022), respectively. Therefore, the wheat N diagnosis status at the Xinghua county can be evaluated based on the indirect NNI diagnosis model and in-season S2 imagery (Fig. 4j).

$$\mathrm{NNI} = \mathrm{Predicted\ PNA}/(\mathrm{Predicted\ PDM} * \mathrm{N}_c) \quad (7)$$

The packages of 'randomForest', 'glmnet', 'nnet' and 'pls' from R software were used during the process of model construction and validation. The determination of wheat growing area at the Xinghua county referenced the research results from Yang et al. (2022). The ArcGIS 10.2 software was used to generate the growth and N status maps in each farm and for Xinghua county. The correlation map and scatter diagram in this study were plotted in the Origin 2021 software.

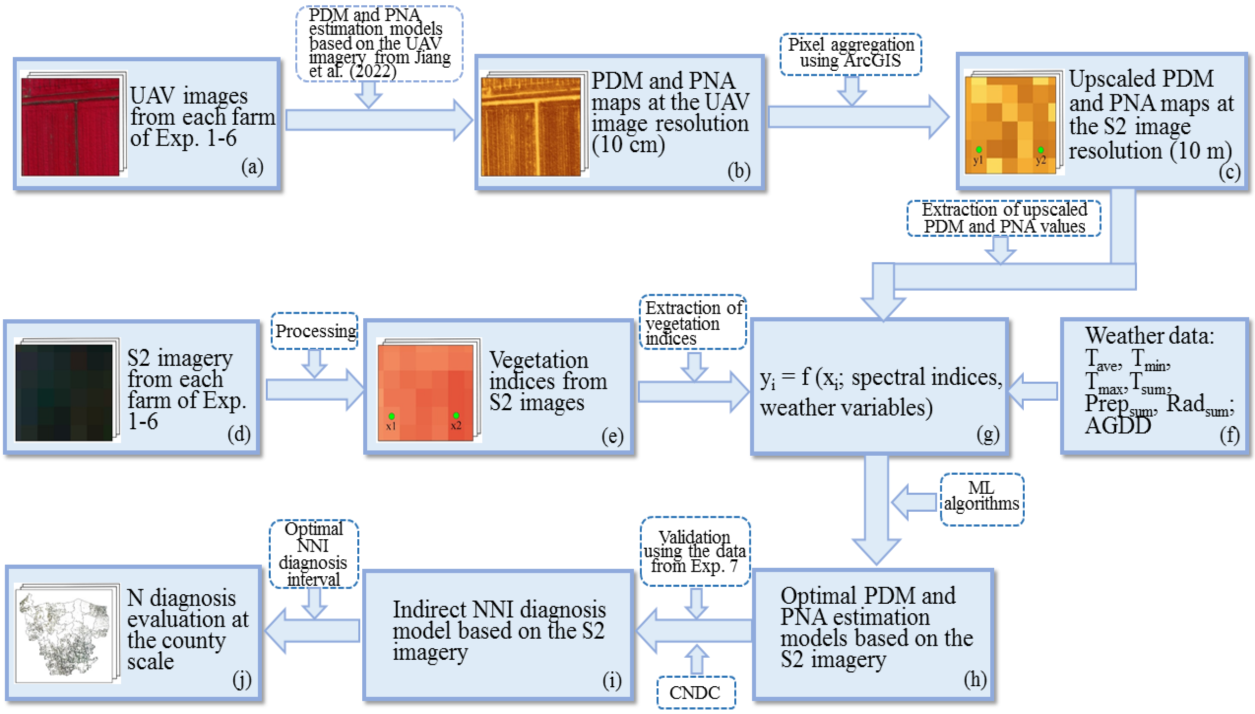

Fig. 4. The research methodology. NNI: N nutrition index; PDM: plant dry matter; PNA: plant N accumulation; S2: Sentinel 2; ML: machine learning; CNDC: critical N dilution curve; T_{ave}, T_{min}, T_{max}, T_{sum}, $Prep_{sum}$ and Rad_{sum} represent the average daily temperature, average daily minimum temperature, average daily maximum temperature, accumulated daily average temperature, accumulated precipitation and accumulated radiation, respectively, of the 30 days before the measurement date. AGDD represents the accumulated growing degree day from sowing to the measurement date. Fig. 4b and c represent the PNA maps that used as an example. The x1, x2 in Fig. 4e represent the sampling points for the extraction of vegetation indices from the S2 imagery, while the y1, y2 in Fig. 4c represent the sampling points for the extraction of upscaled PNA from the upscaled PNA maps.

3. Results

3.1. The correlation of spectral data between UAV and S2 images

The UAV images with 10 cm spatial resolution from experiments 1-6 were resampled (pixel aggregation) to grids that matched the S2 image resolution. Then, the band reflectance derived from the UAV and satellite sensor images were used to calculate the spectral indices in Table 3. A correlation analysis (Fig. 5a) between spectral data derived from the UAV images and the S2 images was performed at the jointing stage. The results showed that the G band from the UAV images, SWIR1 band and DATT vegetation index from the S2 images produced a relatively small correlation (r < 0.50), while most spectral bands and vegetation indices achieved a larger correlation between UAV and S2 spectral data (r > 0.60). The correlation between the UAV and S2 spectral data across the booting stage was generally smaller than that at the jointing stage. However, most vegetation indices produced a well correlation between the UAV and S2 spectral data at the booting stage (Fig. 5b). As a result, the relatively large correlation between the UAV and satellite sensor images can be the basis for the integration of UAV and S2 data.

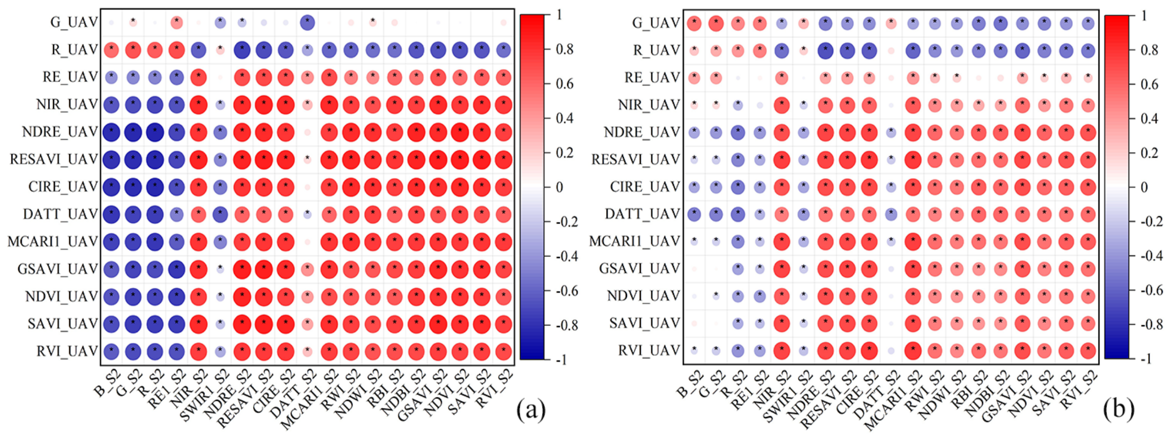

(a) (b)

Fig. 5. The correlation (*r*) of spectral data: between UAV and S2 images at the jointing (a) and booting (b) stages across experiments 1-6. Note: * means a significant difference at the 0.05 probability level. The 'Spectral band_UAV' and 'Vegetation index_UAV' represent the spectral band and vegetation index, respectively, derived from the UAV imagery. The 'Spectral band_S2' and 'Vegetation index_S2' represent the spectral band and vegetation index, respectively, derived from the Sentinel-2 sensor imagery.

3.2. Upscaling the PDM and PNA maps based on pixel aggregation

Diaoyu farm in experiment 3 was used as an example. Seven vegetation indices (Table 3) were calculated using the reflectance from the UAV multispectral images. Fig. 6(a) shows the NDRE (0.11-0.55) maps at the UAV image resolution (10 cm), revealing a large variance in wheat growth across the whole farm. According to the UAV model for PDM and PNA estimation from Jiang et al. (2022), the PDM (Fig. 6b; UAV-PDM) and PNA (Fig. 6c; UAV-PNA) maps with 10 cm resolution were calculated based on the seven vegetation indices extracted from the UAV images, which had a range of 0.64-7.14 t ha^{-1} and 17.71-263.70 kg ha^{-1}, respectively, at the jointing stage across Diaoyu farm. Then, the UAV-PDM (UAV-PNA) maps were upscaled to grids with the same spatial resolution as S2 images (10 m) based on the pixel aggregation. The upscaled PDM (Fig. 6d) and PNA (Fig. 6e) maps had a range of 1.19-5.96 t ha^{-1} and 28.70-216.41 kg ha^{-1}, respectively. Then, 57 sampling points were determined randomly to extract the upscaled PDM and PNA values for calibrating the satellite estimation models.

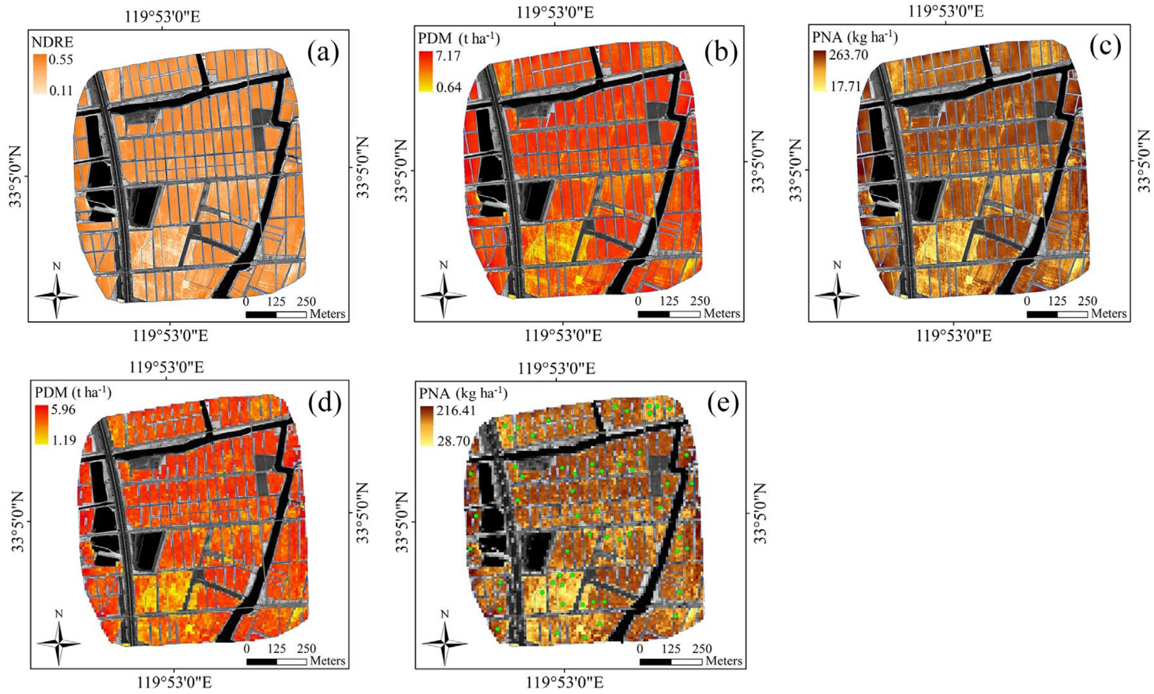

Fig. 6. The NDRE map with (a) UAV (10 cm) image resolution; the PDM maps with (b) UAV (10 cm) and (d) S2 (10 m) image resolution; and the PNA maps with (c) UAV (10 cm) and (e) S2 (10 m) image resolution for Diaoyu farm in experiment 3 at the jointing stage. Note: the green points in Fig. 6(e) represent the randomly determined sampling points.

The statistical analysis was performed for the upscaled PDM and upscaled PNA at the jointing and booting stages in experiment 1-6. The results from the table 4 showed the upscaled PDM and upscaled PNA varied greatly across six experiments. The upscaled PDM ranged from 1.05 to 5.71 with the coefficient of variation (CV) of 46.05% at the jointing stage, and from 2.99 to 6.08 with the CV of 18.59% at the booting stage. Similarly, the upscaled PNA ranged from 24.93 to 136.39 with the CV of 40.18% at the jointing stage, and from 55.32 to 164.89 with the CV of 29.27% at the booting stage. The large variability in the upscaled PDM and PNA renders the dataset suitable to evaluate the performance of using satellite remote sensing information to diagnose winter wheat N status.

Table 4 Descriptive statistics of upscaled plant dry matter (PDM) and plant N accumulation (PNA) at the jointing and booting stages across experiments 1-6.

Parameter	Growth stage	N	Min.	Max.	SD[a]	CV[b] (%)
Upscaled PDM	Jointing	277	1.05	5.71	1.69	46.05
(t ha^{-1})	Booting	240	2.99	6.08	0.92	18.59
Upscaled PNA	Jointing	277	24.93	136.39	34.22	40.18
(kg ha^{-1})	Booting	240	55.32	164.89	32.20	29.27

Note: SD[a] indicates standard deviation of the mean; CV[b] indicates coefficient of variation (%).

3.3. PDM and PNA estimation based on the S2 satellite sensor images

The PDM and PNA values were extracted from the upscaled PDM and PNA maps, respectively. Meanwhile, 13 vegetation indices (Table 3) were calculated based on the reflectance derived from the S2 images. Four ML methods were fitted to the relationship between the upscaled PDM, weather data and 13 spectral indices in the jointing and booting stages. The results from 10-fold cross-validation (Table 5) indicated that the RF method predicted PDM with a high accuracy among the four ML methods. The RF model based on the S2 images achieved an R^2 of 0.93 and 0.69, RMSE of 0.43 and 0.51 t ha^{-1}, and RE of 17.02% and 12.33% in the jointing and booting stage, respectively. Therefore, the RF method was selected as the PDM prediction model across experiments 1-6. Independent data from experiment 7 were used to validate the PDM prediction model based on the RF method. The results show that the PDM model based on the S2 images produced an R^2 of 0.65 and 0.42, RMSE of 0.71 and 0.59 t ha^{-}

^{1}, and RE of 33.85% and 11.65% in the jointing and booting stage, respectively (Table 6).

Similarly, the four ML methods were fitted to the relationships between the upscaled PNA, weather data and spectral indices derived from the S2 images. The 10-fold cross-validation shows that the RF method achieved accurate prediction of PNA among the four ML methods (Table 5). The RF model had an R^2 of 0.77 and 0.60, RMSE of 16.35 kg ha^{-1} and 20.41 kg ha^{-1}, and RE of 24.52% and 20.69% in the jointing and booting stage, respectively. Therefore, the RF method was selected as the PNA prediction model across experiments 1-6. Independent data from experiment 7 were used to validate the PNA prediction model using the RF algorithm. The results show that PNA model based on the S2 images had an R^2 of 0.72 and 0.70, RMSE of 13.40 and 19.05 kg ha^{-1}, and RE of 31.54% and 15.15% at the jointing and booting stage, respectively (Table 6).

Based on the criterion of InNodePurity from the RF model, the relative importance of each input parameter for PDM and PNA estimation can be evaluated (Fig. 7). Generally, the spectral indices have a relatively higher importance than the weather variables for predicting the PDM and PNA. The Rad_{sum}, T_{ave} and AGDD were more important variables for PDM estimation among seven weather parameters at the jointing and booting stages. The variables of T_{max} and AGDD performed a relatively higher importance than other weather parameters for PNA estimation at the jointing and booting stages.

Table 5 The 10-fold cross-validation results across experiments 1-6 using the four ML algorithms at the jointing and booting stages: for the relationship between PDM, weather data and 13 vegetation indices from S2 images; and for relationship between PNA, weather data and 13 vegetation indices from S2 images.

Parameter	Method	Jointing stage			Booting stage		
		R^2	RMSE	RE (%)	R^2	RMSE	RE (%)
PDM	RF	0.93	0.43	17.02	0.69	0.51	12.33
(t ha^{-1})	Lasso	0.93	0.44	17.1	0.67	0.53	12.64
	ANN	0.92	0.51	19.3	0.56	0.71	16.45
	PLSR	0.83	0.69	36.85	0.36	0.74	18.64
PNA	RF	0.77	16.35	24.52	0.60	20.41	20.69
(kg ha^{-1})	Lasso	0.72	18.11	27.31	0.52	22.31	22.27
	ANN	0.63	23.05	30.74	0.42	23.90	25.95
	PLSR	0.61	21.38	35.67	0.34	25.93	26.06

Table 6 Independent validation results of optimal PDM and PNA prediction model using the field data from experiment 7 at the jointing and booting stages.

Parameter	Jointing stage			Booting stage		
	R^2	RMSE	RE (%)	R^2	RMSE	RE (%)
PDM (t ha^{-1})	0.65	0.71	33.85	0.42	0.59	11.65
PNA (kg ha^{-1})	0.72	13.40	31.54	0.70	19.05	15.15

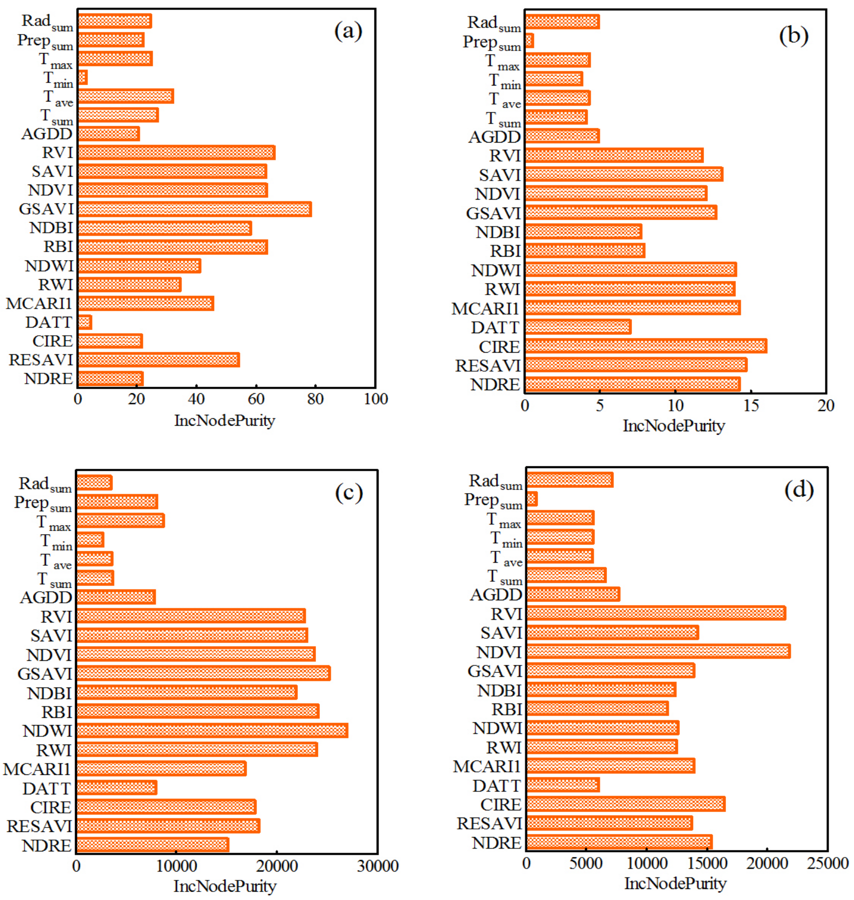

Fig. 7. The importance (InNodePurity) value of each input parameter from the RF model for PDM estimation at the (a) jointing and (b) booting stages; for PNA prediction at the (c) jointing and (d) booting stages.

The above analysis showed the model based on the S2 satellite images performed an accurate prediction for wheat PDM and PNA. Therefore, the S2 estimation model was used to estimate the PDM and PNA at the county scale. The Fig. 8 showed the wheat PDM value had a range of 1.51-4.35 and 3.77-5.85 t ha^{-1} in the jointing (Fig. 8a) and booting (Fig. 8b) stage, respectively; while the PNA value had a range of 34.45-120.86 and 68.18-154.33 kg ha^{-1} in the jointing (Fig. 8c) and booting (Fig. 8d) stage, respectively, across the Xinghua county in 2020-2021.

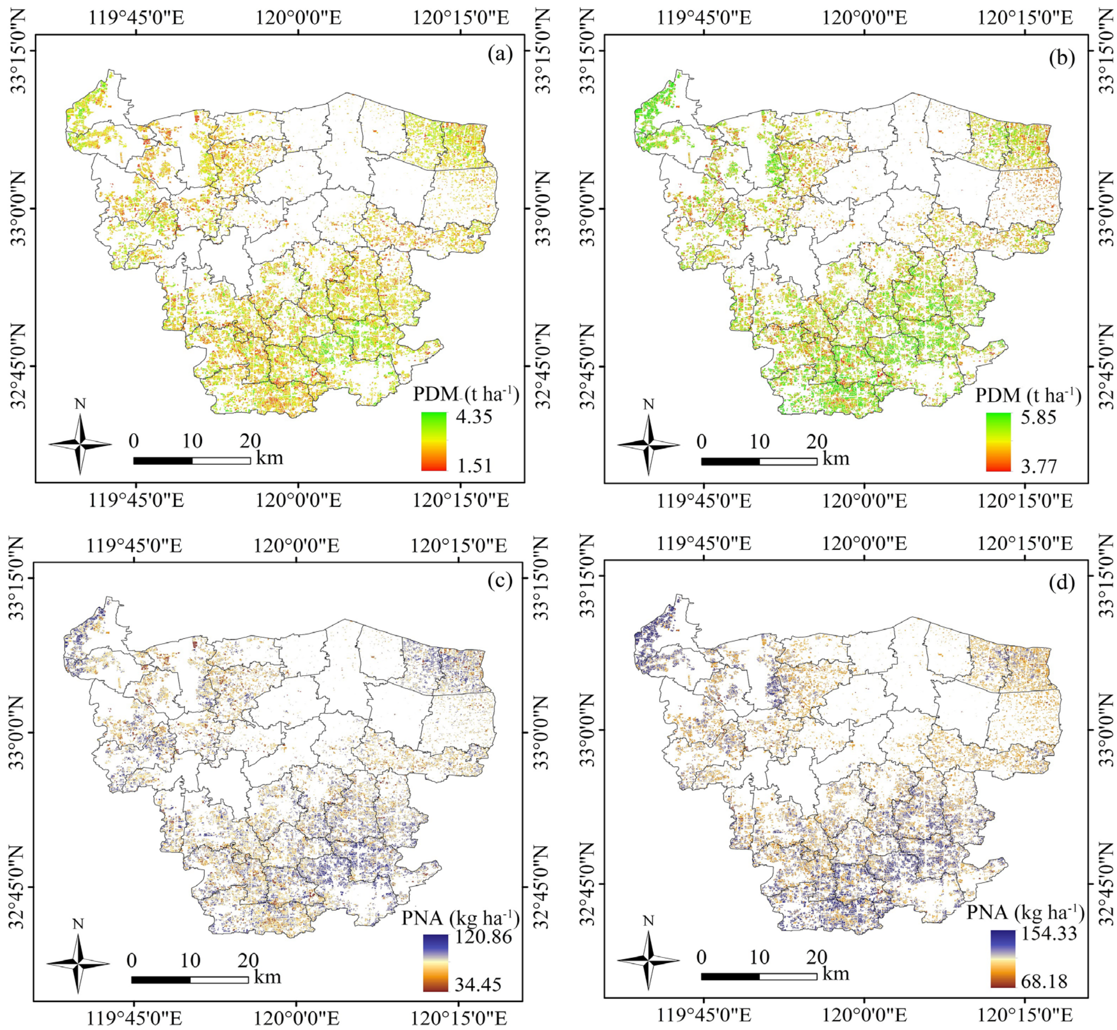

Fig. 8. Maps of PDM at the (a) jointing and (b) booting stages and PNA at the (c) jointing and (d) booting stages based on S2 images in 2020-2021 across Xinghua county.

3.4. N nutrition diagnosis based on NNI at the county scale

After the PDM and PNA were predicted, PNA_c was calculated from the predicted PDM and N_c. Then, the NNI was derived as predicted PNA/PNA_c. Compared to the observed values of NNI from experiment 7, the results show the NNI estimation model based on the S2 images had an R^2 of 0.54 and 0.46, RMSE of 0.12 and 0.13, and RE of 11.80% and 11.85% in the jointing (Fig. 9a) and booting (Fig. 9b) stage, respectively.

The model based on the S2 images was used to predict the NNI at the county scale. According to the optimal NNI diagnosis interval of 0.92-1.04 and 0.97-1.15 in the jointing and booting stage, respectively. Fig. 10a shows that the wheat N status had areas of 21.14%, 42.58%, and 36.28% in the N deficient, optimal and excessive categories, respectively, at the jointing stage; while the proportions of N deficient, optimal and excessive category were 34.35%, 53.87% and 11.78%, respectively, at the booting stage (Fig. 10b) for Xinghua county in 2020-2021.

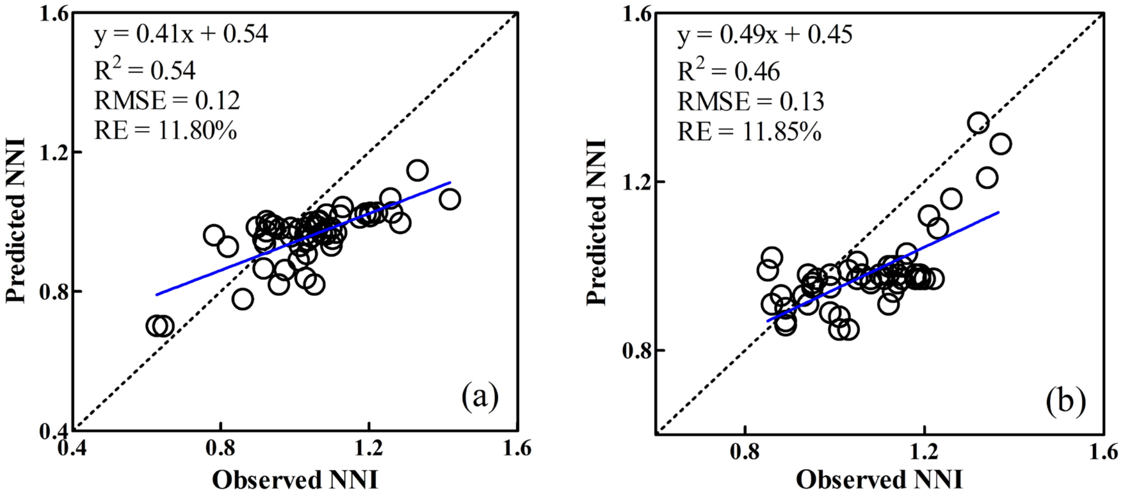

Fig. 9. Independent validation results of NNI prediction model using the field data from experiment 7 at the jointing (a) and booting (b) stages. Note: the blue line in the figure indicates the regression line.

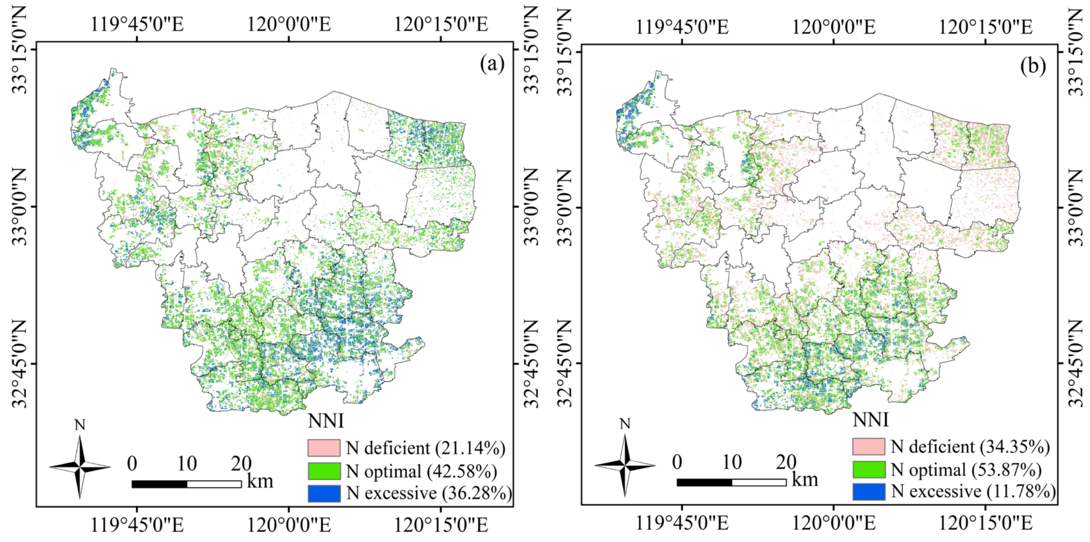

Fig. 10. The N diagnosis maps based on S2 images at the (a) jointing and (b) booting stages across the Xinghua county scale in 2020-2021.

To further evaluate the performance of the satellite-based models and NNI diagnosis maps in experiment 7, a linear relationship was established between grain yield and predicted NNI derived from the NNI estimation model and N diagnosis map of Xinghua county (Fig. 11). The results indicated that the correlation between wheat yield and predicted NNI has R^2 of 0.43 and 0.47 in the jointing (Fig. 11a) and booting (Fig. 11b) stage, respectively.

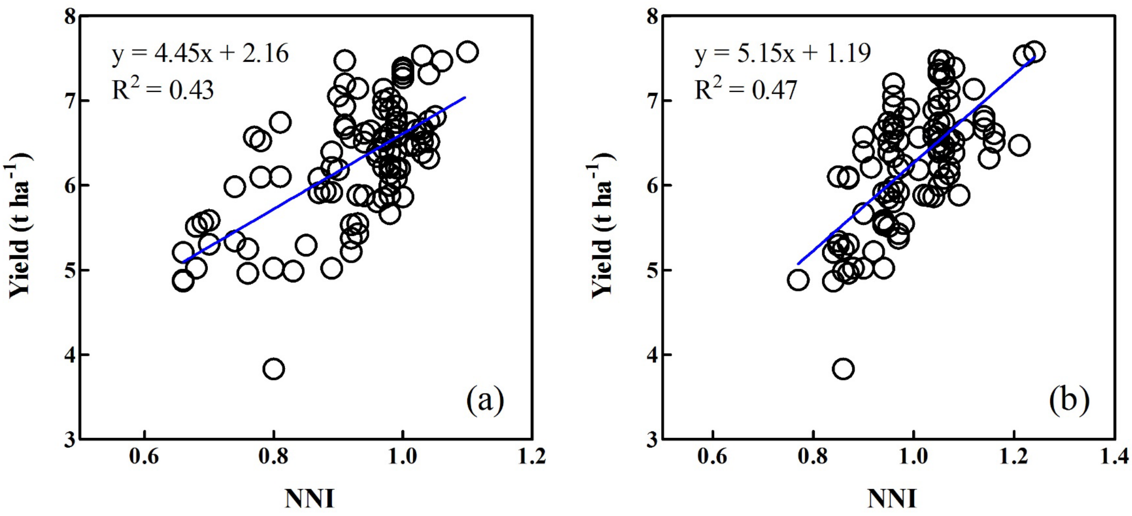

Fig. 11. The linear relationship between wheat yield and predicted NNI from the N diagnosis maps of the Xinghua county at the jointing (a) and booting (b) stage in 2020-2021.

4. Discussion

4.1. Closing the gap between the field observation and satellite data based on the fine resolution UAV images

Crop growth observation is relatively simple at the field scale, but the laborious plant measurement across large areas is more challenging. Therefore, satellite remote sensing can play a significant role for sampling crop information across large areas (Guay et al., 2014). Single or multiple field measurement methods are commonly used to calibrate satellite-based models for crop growth monitoring, which is time-consuming in terms of non-destructive plant sampling. Meanwhile, it is difficult to match the satellite sensor images and field observations at the same spatial resolution (Huang et al., 2017). Fine-resolution UAV images offer the possibility for producing crop growth maps at multiple scales, hence providing a much needed link between field and satellite sensor data. Previous studies showed that tundra vegetation can be classified based on UAV RGB ortho-mosaics in the arctic, which were further converted to Planet (3 m), S2 (10 m, 20 m) and Landsat 8 (30 m) image grids to train satellite-based models for vegetation cover monitoring (Riihimäki et al., 2019). The UAV model of Jiang et al. (2022) achieved a high accuracy for predicting wheat PDM (R^2 = 0.69-0.93) and PNA (R^2 = 0.83-0.84) at the farm scale. Therefore, the PDM

(0.64-7.17 t ha^{-1}) and PNA (17.71-263.70 kg ha^{-1}) values at Diaoyu farm of experiment 3 can be derived from the UAV prediction model (Fig. 6b and 6c, respectively), showing visually the large variability of wheat growth across the whole farm. Furthermore, the PDM maps (0.64 -7.17 t ha^{-1}) with UAV image resolution were upscaled to the S2 image resolution, while the range of PDM decreased with an increase in pixel size, as expected. The upscaled PDM maps with 10 m resolution had values of 1.19-5.96 t ha^{-1}. This aggregation effect arises as part of the well-known Modifiable Areal Unit Problem (MAUP). Previous studies indicated that the phenomenon will arise when finer resolution data are aggregated to coarser spatial resolution (Dark and Bram, 2007), and similar results were demonstrated by Riihimäki et al. (2019). The UAV-PDM (PNA) values with large variability over the farm can be used as reference data for satellite-based model construction. Revill et al. (2020) derived wheat LAI maps from the UAV model, which were then upscaled to S2 grids to train satellite-based estimation models, similar to this study. The co-registration error caused by the GPS deviation between the UAV-derived maps and satellite sensor images should be considered during the analysis process. Therefore, a certain number of control points were set at each farm to calibrate the UAV ortho-mosaics to ensure the accuracy of geographic location. Additionally, more UAV and satellite sensor images from different cultivars and eco-sites should be collected to construct robust models for crop growth prediction and N diagnosis.

4.2. Wheat growth prediction and N diagnosis models based on satellite multi-spectral information and weather variables

Previous studies demonstrated that multi-source information based on spectral indices can increase the accuracy of crop growth and N status prediction, while ML has been found highly suitable for integrating multi-source data (Wang et al., 2021). In this research, four ML methods were used to combine satellite spectral indices and weather data. The RF performed most accurately for predicting PDM (R^2 = 0.42-0.65) and PNA (R^2 = 0.70-0.72), which are comparable to the results of Jiang et al. (2022) who also increased the accuracy of PDM (R^2 = 0.52-0.68) and PNA (R^2 = 0.67-0.82) prediction with the integration of UAV spectral indices, weather and field management data based on the RF method. Nevertheless, the field management data such as N application rates were not considered in this research due to the difficulty of determining it in the different fields over large areas. Although the weather variables play a relatively low importance for PDM and PNA estimation (Fig. 7). However, the changes for radiation and precipitation were reported to affect the crop growth and N nutrition status through adjusting ambient conditions such as air humidity and temperature, which can influence plant stomatal conductance, water status and other physiological functions that control the plant root N absorption and transfer (Naylor et al., 2020; Nonhebel, 1994). Temperature information like AGDD performed a relatively high importance for PDM and PNA estimation (Fig. 7), which may due to the AGDD represent the heat accumulation during the crop growth period, and directly affect to plant growth rate and phenological process (Santos et al., 2021; Zhou et al., 2020). Similar research was conducted by Wang et al., 2021 who integrate the ground sensing information and weather variables such as accumulated precipitation and growing degree day for accurately monitoring the maize NNI and grain yield at V8-V9 growth stage. Additionally, six bands (B, G, R, RE, NIR and SWIR) extracted from the S2 images were used to construct the prediction model in this study. Abundant spectral information was demonstrated to be more representative for characterizing crop growth and N nutrition (Verrelst et al., 2012; 2015). Li et al. (2021) also indicated the integration of multi-source information from S2 images increased the accuracy of chlorophyll prediction across typical lakes in China, similar with those presented in this study. Several studies indicated RF method exhibits a significant performance to integrate the multi variables for predicting plant biomass, leaf area index, and N concentration in wheat, rice, and soybean crops (Muharam et al., 2021; Liang et al., 2018; Maimaitijian et al., 2020). During the RF model construction, multiple sample sub-sets can be obtained from the original sample sets using the bootstrap re-sampling method, while each sample subset was used to construct an independent decision tree for model prediction. Therefore, the fusion of predictions from multiple decision trees was used as the final results of RF models. The specificity of re-sampling and multiple decision trees was demonstrated to well process the outliers during the model construction and improve the model prediction accuracy (Svetnik et al., 2003).

The PDM and PNA prediction accuracies at the booting stage (R^2 = 0.34-0.69) were lower than at the jointing stage (R^2 = 0.61-0.93), which may be due to the influence of wheat canopy closure at the later growth stages (Cao et al., 2015). At the booting stage, the winter wheat grows strongly and all leaves are grown out from the plant. Meanwhile, the top leaves shelter the lower leaves and stem, which limits detection of the whole plant using spectral sensors. Other researchers also demonstrated this similar phenomenon when estimating aboveground biomass and N uptake of rice and wheat leaf area index during the later growth stages (Cao et al., 2013; Zhang et al., 2019). The harvest yield validation for the NNI prediction model and N diagnosis maps achieved a comparable result at the jointing (R^2 = 0.43) and booting (R^2 = 0.47) stages, which was similar with results from Crema et al. (2020) who demonstrated a relationship between S2 image-derived NNI and maize yield with a correlation coefficient r of 0.6. During the practical production, more factors affected the crop growth and yield formation, including fertilizers other than N, water status, soil nutrition, and insect pests and weeds, etc. These useful information should also be considered in model construction to increase the diagnosis accuracy in future study.

4.3. The potential for Sentinel 2 to diagnose crop N status across large areas

Satellite remote sensing has great potential for predicting crop growth across large areas due to the larger sampling extent than ground-based and aerial spectral sensing systems (Zhang et al., 2020). Previous studies used satellite sensor images for applied predicting crop LAI, aboveground biomass and N content in wheat at the farm scale (Li et al., 2019; Fabbri et al., 2020), while not for diagnosing N status across larger areas such as a county. In this research, S2 images with swath widths of 240 km were demonstrated to provide large area crop information compared to the small image swath widths of, for example, the Planet mission (24.6 km; Li et al., 2019). Generally, the fine spatial resolution images were demonstrated to involve more crop information than at coarser resolution. However, this also necessitates complex calculations during data analysis when used for practical applications. On the other hand, coarse spatial resolution images such as from Landsat (30 m) cannot detect field heterogeneity, especially as most of the fields studied here are approximately 40 m wide. Thus, medium resolution sensors such as Landsat are not suitable for developing crop management strategies in each field (Huang et al., 2017) . In this regard, it was implicit that the S2 images with medium-fine resolution were more feasible for characterising crop N nutrition status and guiding N nutrition management at the county scale. Areas of 36.28% and 21.14% belong to the N excessive and deficient categories, respectively, at the jointing stage, which means less and more N demand, respectively, compared to the optimal N status (Fig. 10a). However, an area of 34.35% of the N deficient category was found at the booting stage, which may due to inappropriate topdressing N application by farmers across the whole county (Fig. 10b). Therefore, a suitable N regulation algorithm should be developed to adjust N topdressing rates on the basis of farmers' N management at the jointing stage. Previous studies showed the PNMS supported by UAV remote sensing data optimized crop growth and improved the NUE for wheat production (Argento et al., 2021), while the relevant PNMS based on satellite sensor images should also be developed and applied at the county scale. The crop growth stage may vary over such a large area, and it is unwise to apply the same management strategy to crops under different growth stages. As a result, the influence of the growth stage should be considered for crop N status diagnosis and regulation. Previous studies demonstrated that the synthetic aperture radar (SAR) and optical time-series data derived from the satellite and UAV remote sensing systems have been used for accurately tracking the crop phenological phrase in rice, winter wheat, maize and soybean (Diao et al., 2021; Liu et al., 2022; Guo et al., 2022; Zhao et al., 2022). Therefore, the integration of crop phenology estimation technology and N management strategy may better facilitate to most precisely diagnose the crop N status and determine the optimal N recommendation rates at the optimal growth stages, which would be significant for improving the crop growth and increasing the N use efficiency. However, the difference in growth period for winter wheat was not more than 5 days in Xinghua county according to the survey. Therefore, the growth stages were regarded as uniform across the whole county and the influence of growth stage was not considered during model construction in this study. Nevertheless, it should be considered for larger areas in future studies.

5. Conclusion

This research demonstrated the farm-scale PDM (UAV-PDM) and PNA (UAV-PNA) maps derived from fine-resolution UAV images can be aggregated to grids that match the S2 satellite image resolution to calibrate satellite-based models for wheat growth and N status estimation. Meanwhile, the results indicated that the S2 imagery-derived model based on the RF algorithm produced a high accuracy for predicting the PDM, PNA and NNI in the jointing and booting stages. Thereby, wheat growth and N nutrition status were mapped across Xinghua county, China. We conclude that the combination of UAV and satellite images can be used to diagnose and map wheat growth and N status across wide areas (the county scale).

Funding

This work was supported by the National Key Research and Development Program of China (No. 2022YFD2301402), the National Natural Science Foundation of China (No. 32071903), the Jiangsu Provincial Key Technologies R&D Program of China (No. BE2019386), and the Guidance Foundation the Sanya Institute of Nanjing Agricultural University (No. NAUSY-ZD01), China.

CRediT authorship contribution statement

Jie Jiang: Conceptualization, Methodology, Formal analysis, Software, Formal analysis, Investigation, Writing–original draft, Visualization. **Peter M. Atkinson:** Methodology, Writing–review & editing. **Chunsheng Chen:** Methodology, Investigation. **Qiang Cao:** Methodology, Investigation. **Yongchao Tian:** Methodology, Writing–review & editing. **Yan Zhu:** Investigation, Writing–review & editing. **Xiaojun Liu:** Conceptualization, Methodology, Supervision, Funding acquisition, Writing–review & editing. **Weixing Cao:** Supervision, Funding acquisition, Writing–review & editing.

Declaration of Competing Interest

The authors declare that they have no known competing financial interests or personal relationships that could have appeared to influence the work reported in this paper.

Acknowledgments

Thanks to Xue Wang, Jiayi Zhang, Zhihao Zhang, Yang Gao, Xinge Li for field

management, ground measurement, and chemical analysis of plant samples.

Conflicts of Interest

The authors declare no conflict of interest.

Reference

Argento, F., Anken, T., Abt, F., Vogelsanger, E., Walter, A., Liebisch, F., 2021. Site-specific nitrogen management in winter wheat supported by low-altitude remote sensing and soil data. Precis. Agric. 22, 364–386. https://doi.org/10.1007/s11119-020-09733-3.

Barnes, E.M., Clarke, T.R., Richards, S.E., Colaizzi, P.D., Thompson, T., 2000. Coincident detection of crop water stress, nitrogen status, and canopy density using ground based multispectral data. Proc. 5th Int. Conf. Precis. Agric. Other Resour. Manag. 16–19 (Bloomington, MN, USA).

Bremner, J., Mulvaney, C., 1982. In: Miller, R.H., A.L., Keeney, D.R. (Eds.), Nitrogen -total. In Methods of Soil Analysis. In Chemical and Microbial Properties. American Society of Agronomy, and Soil Science Society, Madison, WI, USA, pp. 595–624.

Cao, Q., Miao, Y., Wang, H., Huang, S., Cheng, S., Khosla, R., Jiang, R., 2013. Non-destructive estimation of rice plant nitrogen status with Crop Circle multispectral active canopy sensor. Field Crops Res. 154, 133–144. https://doi.org/10.1016/j.fcr.2013.08.005.

Cao, Q., Miao, Y., Feng, G., Gao, X., Li, F., Liu, B., Yue, S., Cheng, S., Ustin, S.L., Khosla, R., 2015. Active canopy sensing of winter wheat nitrogen status: An evaluation of two sensor systems. Comput. Electron. Agric. 112, 54–67. https://doi.org/10.1016/j.compag.2014.08.012.

Crema, A., Boschetti, M., Nutini, F., Cillis, D., Casa, R., 2020. Influence of Soil Properties on Maize and Wheat Nitrogen Status Assessment from Sentinel-2 Data. Remote Sens. 12, 2175. https://doi.org/10.3390/rs12142175.

Dark, S.J., Bram, D., 2007. The modifable areal unit problem (MAUP) in physical geography. Prog. Phys. Geogr. 31, 471–479. https://doi.org/10.1177/0309133307083294.

Datt, B., 2010. Visible/near infrared reflectance and chlorophyll content in Eucalyptus leaves. Int. J. Remote Sens. 20, 2741–2759. https://doi.org/10.1080/014311699211778.

Diacono, M., Montemurro, F., 2013. Precision nitrogen management of wheat. A review. Agron. Sustain. Dev. 33, 219–241. https://doi.org/10.1007/s13593-012-0111-z.

Diao, C., Yang, Z., Gao, F., Zhang, X., Yang, Z., 2021. Hybrid phenology matching model for robust crop phenological retrieval. ISPRS J. Photogramm. Remote Sens. 181, 308–326. https://doi.org/10.1016/j.isprsjprs.2021.09.011.

Dong, T., Shang, J., Chen, J.M., Liu, J., Zhou, G., 2019. Assessment of portable chlorophyll meters for measuring crop leaf chlorophyll concentration. Remote Sens. 11, 2706. https://doi.org/10.3390/rs11222706.

Fabbri, C., Mancini, M., Marta, A.D., Orlandini, S., Napoli, M., 2020. Integrating satellite data with a Nitrogen Nutrition Curve for precision top-dress fertilization of durum wheat. Eur. J. Agron. 120, 126148 https://doi.org/10.1016/j.eja.2020.126148.

Fernandes, R., Butson, C., Leblanc, S., Latifovic, R., 2003. Landsat-5 TM and landsat-7 ETM +based accuracy assessment of leaf area index products for Canada derived from SPOT-4 VEGETATION data. Can. J. Remote Sens. 29, 241–258. https://doi.org/ 10.5589/m02-092.

Gao, B., 1995. NDWI—A normalized difference water index for remote sensing of vegetation liquid water from space. Remote Sens. Environ. 58, 257–266. https://doi. org/10.1016/S0034-4257(96)00067-3.

Gitelson, A.A., Vin˜a, A., Ciganda, V., Rundquist, D.C., Arkebauer, T.J., 2005. Remote estimation of canopy chlorophyll content in crops. Geophys. Res. Lett. 32, 1–4. https://doi.org/10.1029/2005GL022688.

Guay, K., Beck, P., Berner, L., Goetz, S., Baccini, A., Buermann, W., 2014. Vegetation productivity patterns at high northern latitudes: A multi-sensor satellite data assessment. Glob. Change Biol. 20, 3147–3158. https://doi.org/10.1111/gcb.12647.

Guo, Y., Xiao, Y., Li, M., Hao, F., Zhang, X., Sun, H., Beurs, K., Fu, Y., He, Y., 2022. Identifying crop phenology using maize height constructed from multi-sources images. Int. J. Appl. Earth Obs. Geoinf. 115, 103121 https://doi.org/10.1016/j. jag.2022.103121.

Huang, S., Miao, Y., Yuan, F., Martin, G., Yao, Y., Cao, Q., Wang, H., Victoria, L.W., Georg, B., 2017. Potential of RapidEye and WorldView-2 Satellite Data for Improving Rice Nitrogen Status Monitoring at Different Growth Stages. Remote Sens. 9, 227. https://doi.org/10.3390/rs9030227.

Huete, A., 1988. A soil adjusted vegetation index (SAVI). Remote Sens. Environ. 17, 37–53. https://doi.org/10.1016/0034-4257(88)90106-X.

Jiang, J., Wang, C., Wang, Y., Cao, Q., Liu, X., 2020. Using an active sensor to develop new critical nitrogen dilution curve for winter wheat. Sensors 20, 1577. https://doi.org/10.3390/s20061577.

Jiang, J., Peter, M., Zhang, J., Lu, R., Zhou, Y., Cao, Q., Tian, Y., Zhu, Y., Cao, W., Liu, X., 2022. Combining fixed-wing UAV multispectral imagery and machine learning to diagnose winter wheat nitrogen status at the farm scale. Eur. J. Agron. 138, 126537 https://doi.org/10.1016/j.eja.2022.126537.

Lepine, L., Ollinger, S., Ouimette, A., Martin, M., 2016. Examining spectral reflectance features related to foliar nitrogen in forests: Implications for broad-scale nitrogen mapping. Remote Sens. Environ. 173, 174–186. https://doi.org/10.1016/j.rse.2015.11.028.

Li, K., Yang, X., Tian, H., Pan, S., Liu, Z., Lu, S., 2016. Effects of changing climate and cultivar on the phenology and yield of winter wheat in the North China Plain. Int. J. Biometeorol. 60 (1), 21–32. https://doi.org/10.1007/s00484-015-1002-1.

Li, S., Song, K., Wang, S., Liu, G., Mu, G., 2021. Quantification of chlorophyll-a in typical lakes across China using Sentinel-2 MSI imagery with machine learning algorithm. Sci. Total Environ. 778, 146271 https://doi.org/10.1016/j.scitotenv.2021.146271.

Li, W., Jiang, J., Guo, T., Zhou, M., Yao, X., 2019. Remote sensing Generating Red-Edge Images at 3 M Spatial Resolution by Fusing Sentinel-2 and Planet Satellite Products. Remote Sens. 11, 1422. https://doi.org/10.3390/rs11121422.

Liang, L., Di, L., Huang, T., Wang, J., Lin, L., Wang, L., Yang, M., 2018. Estimation of leaf nitrogen content in wheat using new hyperspectral indices and a random forest regression algorithm. Remote Sens. 10, 1940.

Liu, L., Cao, R., Chen, J., Shen, M., Wang, S., Zhou, J., He, B., 2022. Detecting crop phenology from vegetation index time-series data by improved shape model fitting in each phenological stage. Remote Sens. Environ. 277, 277. https://doi.org/ 10.1016/j.rse.2022.113060.

Magney, T.S., Eitel, J.U.H., Vierling, L.A., 2017. Mapping wheat nitrogen uptake from RapidEye vegetation indices. Precis. Agric. 18, 429–451. https://doi.org/10.1007/ s11119-016-9463-8.

Maimaitijiang, M., Sagan, V., Sidike, P., Daloye, A., Erkbol, H., Fritschi, F., 2020. Crop Monitoring Using Satellite/UAV Data Fusionand Machine Learning. Remote Sens. 12, 1357. https://doi.org/10.3390/rs12091357.

Miao, Y., Stewart, B., Zhang, F., 2011. Long-term experiments for sustainable nutrient management in China. A review. Agron. Sustain. Dev. 31, 397–414. https://doi.org/ 10.1051/agro/2010034.

Moya, A.C.A.Z., 2005. Optically assessed contents of leaf polyphenolics and chlorophyll as indicators of nitrogen deficiency in wheat (Triticum aestivum L.).

Field Crops Res. 91, 35–49. https://doi.org/10.1016/j.fcr.2004.05.002.

Muharam, F.M., Nurulhuda, K., Zulkafli, Z., Tarmizi, M.A., Abdullah, A., Hashim, M., Zad, S., Derraz, R., Ismail, M., R., 2021. Uav- and random-forest-adaboost (rfa)-based estimation of rice plant traits. Agronomy 11, 915. https://doi.org/10.3390/agronomy11050915.

Naylor, D., Sadler, N., Bhattacharjee, A., Graham, E.B., Anderton, C.R., McClure, R., Lipton, M., Hofmockel, K.S., Jansson, J.K., 2020. Soil microbiomes under climate change and implications for carbon cycling. Annu. Rev. Environ. Resour. 45, 29–59. https://doi.org/10.1146/annurev-environ-012320-082720.

Nonhebel, S., 1994. The effects of use of average instead of daily weather data in crop growth simulation models. Agric. Syst. 44, 377–396. https://doi.org/10.1016/0308- 521X(94)90194-K.

Padilla, F., Gallardo, M., Pen˜a-Fleitas, M., Souza, R., Thompson, R., 2018. Proximal Optical Sensors for Nitrogen Management of Vegetable Crops: A Review. Sensors 18, 2083. https://doi.org/10.3390/s18072083.

Pearson, R., Miller, L., 1972. Remote Mapping of Standing Crop Biomass for Estimation of Productivity of the Shortgrass Prairie. Oct 2–6 Proceedings of the Eighth International Symposium on Remote Sensing of Environment. Environmental Research Institute of Michigan, Ann Arbor, MI, pp. 1357–1381. https://doi.org/ 10.1177/002076409904500102. Oct 2–6.

Revill, A., Florence, A., Macarthur, A., Hoad, S., Williams, M., 2020. Quantifying Uncertainty and Bridging the Scaling Gap in the Retrieval of Leaf Area Index by

Coupling Sentinel-2 and UAV Observations. Remote Sens. 12, 1843. https://doi.org/ 10.3390/rs12111843.

Riihima¨ki, H., Luoto, M., Heiskanen, J., 2019. Estimating fractional cover of tundra vegetation at multiple scales using unmanned aerial systems and optical satellite data. Remote Sens. Environ. 224, 119–132. https://doi.org/10.1016/j. rse.2019.01.030.

Rinaldi, M., Ruggieri, S., Garofalo, P., Vonella, A.V., Satalino, G., Soldo, P., 2010. Leaf Area Index Retrieval Using High Resolution Remote Sensing Data. Ital. J. Agron. 5, 155–166. https://doi.org/10.4081/ija.2010.155.

Santos, A., Lacerda, L., Rossi, C., Moreno, L., Oliveira, M., Pilon, C., Silva, R., Vellidis, G., 2021. Using UAV and multispectral images to estimate peanut maturity variability on irrigated and rainfed fields applying linear models and artificial neural networks. Remote Sens. 14, 93. https://doi.org/10.3390/rs14010093.

Sharifi, A., 2020. Using Sentinel-2 data to predict nitrogen uptake in maize crop. IEEE J. Sel. Top. Appl. Earth Obs. Remote Sens. 99, 1. https://doi.org/10.1109/ JSTARS.2020.2998638.

Sripada, R.P., Heiniger, R.W., White, J.G., Weisz, R., 2005. Aerial Color Infrared Photography for Determining Late-Season Nitrogen Requirements in Corn. Agron. J. 97, 1511–1514. https://doi.org/10.2134/agronj2004.0314.

Svetnik, V., Liaw, A., Tong, C., Culberson, J., Sheridan, R., Feuston, B., 2003. Random Forest: A Classification and Regression Tool for Compound Classification and QSAR Modeling. J. Chem. Inf. Comput. Sci. 43, 1947–1958.

Tucker, C.J., 1979. Red and photographic infrared linear combinations for monitoring vegetation. Remote Sens. Environ. 8, 127–150. https://doi.org/10.1016/0034-4257(79)90013-0.

Verma, U., Ruhal, D.S., Hooda, R.S., Yadav, M., Hooda, L., 2003. Wheat Yield Modelling Using Remote Sensing and Agrometeorological Data in Haryana State. Indian Soc. Agricult. Stat. (India) 56 (2), 190–198.

Verrelst, J., Mun˜oz, J., Alonso, L., et al., 2012. Machine learning regression algorithms for biophysical parameter retrieval: Opportunities for Sentinel-2 and -3. Remote Sens. Environ. 118, 127–139. https://doi.org/10.1016/j.rse.2011.11.002.

Verrelst, J., Rivera Caicedo, J., Veroustraete, F., Mun˜oz, J., Clevers, J.G.P.W., Camps-Valls, G., Moreno, J., 2015. Experimental Sentinel-2 LAI estimation using parametric, non-parametric and physical retrieval methods – A comparison. ISPRS J. Photogramm. Remote Sens. 108, 260–272. https://doi.org/10.1016/j.isprsjprs.2015.04.013.

Wang, K., Huggins, D.R., Tao, H., 2019. Rapid mapping of winter wheat yield, protein, and nitrogen uptake using remote and proximal sensing. Int. J. Appl. Earth Obs. Geoinf. 82, 101921 https://doi.org/10.1016/j.jag.2019.101921.

Wang, X., Miao, Y., Dong, R., Hainie, Z., Xia, T., Zhichao, C., Kusnierek, K., Mi, G., Sun, H., Li, M., 2021. Machine learning-based in-season nitrogen status diagnosis and side-dress nitrogen recommendation for corn. Eur. J. Agron. 123, 126193 https://doi.org/10.1016/j.eja.2020.126193.

Wu, J.J., Wang, N., Shen, H.Z., Ma, X.Y., 2022. Spatial–temporal variation of climate and its impact on winter wheat production in guanzhong plain, china. Comput. Electron. Agric. 195, 106820 https://doi.org/10.1016/j.compag.2022.106820.

Xia, T., Miao, Y., Wu, D., Hui, S., Khosla, R., Mi, G., 2016. Active optical sensing of spring maize for in-season diagnosis of nitrogen status based on nitrogen nutrition index. Remote Sens. 8, 605. https://doi.org/10.3390/rs8070605.

Yang, G., Yu, W., Yao, X., Zheng, H., Cao, Q., Zhu, Y., Cao, W., Cheng, T., 2021. AGTOC: A novel approach to winter wheat mapping by automatic generation of training samples and one-class classification on Google Earth Engine. Int. J. Appl. Earth Obs. Geoinf. 102, 102446 https://doi.org/10.1016/j.jag.2021.102446.

Zha, H., Miao, Y., Wang, T., Li, Y., Kusnierek, K., 2020. Improving unmanned aerial vehicle remote sensing-based rice nitrogen nutrition index prediction with machine learning. Remote Sens. 12, 215. https://doi.org/10.3390/rs12020215.

Zhang, C., Marzougui, A., Sankaran, S., 2020. High-resolution satellite imagery applications in crop phenotyping: An overview. Comput. Electron. Agric. 175, 105584 https://doi.org/10.1016/j.compag.2020.105584.

Zhang, J., Liu, X., Liang, Y., Cao, Q., Tian, Y., Zhu, Y., Cao, W., Liu, X., 2019. Using a portable active sensor to monitor growth parameters and predict grain yield of winter wheat. Sensors 19, 1108. https://doi.org/10.3390/s19051108.

Zhang, K., Yuan, Z., Yang, T., Lu, Z., Tian, Y., Zhu, Y., Cao, Q., Liu, X., 2020. Chlorophyll meter–based nitrogen fertilizer optimization algorithm and nitrogen nutrition index for in-season fertilization of paddy rice. Agron. J. 112, 288–300. https://doi.org/ 10.1002/agj2.20036.

Zhao, J., Zhang, X., Gao, C., Qiu, X., Cao, W., 2019. Rapid Mosaicking of Unmanned Aerial Vehicle (UAV) Images for Crop Growth Monitoring Using the SIFT Algorithm. Remote Sens. 11, 1226. https://doi.org/10.3390/rs11101226.

Zhao, W., Qu, Y., Zhang, L., Li, K., 2022. Spatial-aware SAR-optical time-series deep integration for crop phenology tracking. Remote Sens. Environ. 276, 113046 https:// doi.org/10.1016/j.rse.2022.113046.

Zhou, M., Ma, X., Wang, K., Cheng, T., Wang, J., Zhu, Y., Wu, Z., Niu, Q., Gui, L., Yue, C., Yao, X., 2020. Detection of phenology using an improved shape model on time-series vegetation index in wheat. Comput. Electron. Agric. 173, 105398 https://doi.org/ 10.1016/j.compag.2020.105398.